An experimental and numerical study of the resonant flow between a hull and a wall

I.A. Milne, O. Kimmoun, J.M.R. Graham, B. Molin

An experimental and numerical study of the resonant flow between a hull and a wall

I. A. Milne[1]†, O. Kimmoun[2], J. M. R. Graham[3] and B. Molin[2]

[1]Oceans Graduate School, The University of Western Australia, Crawley, 6009, Australia
[2]Aix Marseille Univ, CNRS, Centrale Marseille, IRPHE, Marseille, France
[3]Department of Aeronautics, Imperial College London, SW7 2AZ, UK

(Received xx; revised xx; accepted xx)

The wave-induced resonant flow in a narrow gap between a stationary hull and a vertical wall is studied experimentally and numerically. Vortex shedding from the sharp bilge edge of the hull gives rise to a quadratically-damped free surface response in the gap, where the damping coefficient is approximately independent of wave steepness and frequency. Particle image velocimetry (PIV) and direct numerical simulations (DNS) were used to characterise the shedding dynamics and explore the influence of discretisation in the measurements and computations. Secondary separation was identified as a particular feature which occurred at the hull bilge in these gap flows. This can result in the generation of a system with multiple vortical regions and asymmetries between the inflow and outflow. The shedding dynamics were found to exhibit a high degree of invariance to the amplitude in the gap and the spanwise position of the barge. The new measurements and the evaluation of numerical models of varying fidelity can assist in informing offshore operations such as the side by side offloading from Floating Liquid Natural Gas (FLNG) facilities.

Key words: Gap resonance, vortex shedding, hydrodynamic damping

1. Introduction

The resonant flow in the narrow gap between a carrier and a second vessel or a solid terminal often governs operability (Zhao *et al.* 2018). Near resonance, the potential flow damping is small and viscous effects can provide a significant contribution to the total hydrodynamic damping. Compared to the inviscid response, the viscous effects are typically significantly more challenging to determine, such that the free surface amplitudes at resonance are difficult to predict.

Given the practical importance, numerous studies have been carried out to investigate resonances in narrow gaps between vessels and terminals, as well as in moonpools. These have been approached theoretically, numerically and experimentally (see e.g. Faltinsen & Timokha (2015); Zhao *et al.* (2017); Molin *et al.* (2018) and references therein). Such studies have demonstrated how the addition of artificial damping to potential flow solutions, or vortex methods, or viscous solvers with high spatial and temporal resolution are generally required for reliable predictions of the resonant amplitudes. However, the underlying complex flow dynamics around the bilge of the ship and within the gap (or moonpool) which underpins the response remains comparatively less understood.

† Email address for correspondence: ian.milne@uwa.edu.au

Provided that the edge or bilge is sufficiently sharp and the Reynolds number is not small, flow separation occurs and vortex shedding can be expected to have a dominant contribution to the damping over other viscous effects such as skin friction (Kristiansen & Faltinsen 2008; Feng *et al.* 2017). In such cases, the flow dynamics are generally considered to be nearly independent of Reynolds number, with the flow separating at the edge and viscosity only affecting the decay of the shed vortices. However, compared to the flow around an isolated edge, such as the case considered by Graham (1980), for instance, a narrow gap presents additional complexities and gives rise to asymmetries between the oscillatory half-cycles. In particular, the confinement of the flow may be expected to influence the displacement of the vortices which can remain close to the hull and affect the separation, but which has seldom been studied.

Experimentalists have pursued various means to investigate gap and moonpool resonance. The problem has often been simplified by generating idealised two-dimensional flow conditions in a wave tank. Kristiansen & Faltinsen (2008) and Ravinthrakumar *et al.* (2019), for instance, used the forced heave response of two rigidly connected hull sections separated by a small gap to study the moonpool problem. The terminal and side-by-side problems have been investigated using fixed hulls positioned either close to a wall (Kristiansen & Faltinsen 2009) or separated by a small gap (Tan *et al.* 2019), subjected to surface waves. Fewer studies have been performed in wave basins, which although potentially enable realistic hull forms or three-dimensional resonances to be investigated (see e.g. Peri & Swan (2015); Zhao *et al.* (2017)), are less amendable to flow visualisation such as particle image velocimetry (PIV) to study the vortex shedding dynamics.

Experimental studies have also served to provide empirical corrections to inviscid models to enable computationally efficient prediction of the free surface responses in narrow gaps or moonpools, which may facilitate parametric studies. As demonstrated by Kimmoun *et al.* (2011) for a rectangular barge next to a vertical wall, not accounting for flow separation at the bilges results in unrealistically large predictions of the free surface amplitudes when considering the linear diffraction/radiation problems alone. The effect of vortex shedding has typically been treated indirectly within inviscid models by incorporating a fictitious lid in the gap, tuned to provide appropriate (typically quadratic) damping (e.g. Molin *et al.* (2009)). Deploying such models in practice however, requires understanding the universality of the additional viscous correction terms since the data for their determination are generally limited.

The application of viscous or vortex methods is necessary to resolve the underlying flow dynamics and vorticity fields around the bilge and within the gap. Solvers of the unsteady Navier-Stokes equations for three-dimensional multiphase flow have been implemented by Feng *et al.* (2017) and Wang *et al.* (2019) for the pure diffraction response for two identical stationary barges in close proximity. However, significant supercomputing resources are required to fully resolve flow separation which in many cases approximates to two-dimensional flow over extensive lengths of the hull. As such, two-dimensional Navier-Stokes computations are more practical to study the problem and determine the flow field over the entire wave tank as demonstrated by Moradi *et al.* (2015) and Lu *et al.* (2020), for instance. This also avoids possible issues related to the coupling of viscous solvers to capture flow separation with inviscid solutions as pursued by Kristiansen & Faltinsen (2012) and Ravinthrakumar *et al.* (2019). Notably, Lu *et al.* (2020) considered a barge heaving and swaying next to a vertical wall and presented vorticity contours to support the conclusion that vortex shedding around the square bilge dominated the damping of the gap response.

Vortex methods are particularly well suited to predicting flows with well-defined separation points such as sharp-edged bilges. Graham (1980) applied an inviscid, discrete

vortex technique to show that the drag coefficient due to the vortex force for oscillatory flow around an infinite right-angled edge at low Keulegan-Carpenter number (K_C) was independent of K_C. For relatively small gap oscillations where the vortices remain close to the bilge, this would suggest that the damping coefficient is independent of the geometry. A vortex model combined with an inviscid boundary element solution was also used by Kristiansen & Faltinsen (2008) to study the moonpool problem. While vortex models omit diffusion and boundary layer separation, their superior computational efficiency compared to CFD is particularly useful for conducting parametric studies and estimating the vortex contribution to the damping while still encapsulating the rich physics.

To this end, the objectives here are to devise an experiment and appropriate numerical models to study not only the free surface response but also the flow fields around the bilge and within the gap in resonant conditions. Specifically, the intention is to provide new insights on the fundamental flow separation and vortex shedding dynamics and, in turn, the capabilities of PIV and numerical models to investigate the problem and determine the vortex contribution to the hydrodynamic damping. The response associated with regular waves incident to a two-dimensional section of a fixed barge located next to a vertical wall in a wave tank is considered. The setup is regarded as a suitable analogue to common gap resonance scenarios in practice, such as the side by side offloading from Floating Liquid Natural Gas (FLNG) facilities to LNG carriers in the open sea, and appropriate for evaluating the efficacy of PIV and numerical models of varying fidelity.

2. Experiment

2.1. *Facility and set-up*

The experiment was conducted in the wave tank at École Centrale Marseille and the set-up is depicted in figure 1. The wave tank is 0.65 m wide and the vertical wall was positioned at a distance of $L = 12.02$ m from the wavemaker, with the water depth set at $h = 0.52$ m. The hull had a beam of $b = 0.6$ m, draft of $d = 0.12$ m and spanned the width of the tank. The sides of the hull were vertical and the bilges were right-angled (i.e. square edges). For the purposes of this study the hull motion was fully restrained and only the pure diffraction response was considered. The vertical wall extended to the bottom of the tank and the gap between the wall and the barge was $w = 0.073$ m (i.e. $w/b = 0.12$).

The barge model was constructed from 250 mm thick Poly(methyl methacrylate) (PMMA) to provide the required rigidity. The vertical wall was a 25 mm thick Polyvinyl Chloride (PVC) plate. It was affixed to the walls and bottom of the tank as to ensure that it did not deform under the significant hydrodynamic pressures generated during the experiment. All dimensions and angles were confirmed using a mechanics rule, with tolerances of less than 0.5 mm.

The flat-type wavemaker was used to generate regular surface waves of constant wave steepness. A linear ramp function was applied to the wave amplitude for the first three wave periods in order to reduce the effect of initial transients. All measurements were acquired having ensured that the water in the tank was well mixed and the uniformity of the temperature was confirmed regularly using probes. The water surface elevation was measured at several locations upstream of the barge as well as in the gap using resistance wave gauges. With this set-up, based on a typical wave period of $T = 1.1$ s, the reflected wavetrain would be re-encountered at the hull after around $t = 35$ s, providing a sufficient uncompromised test duration.

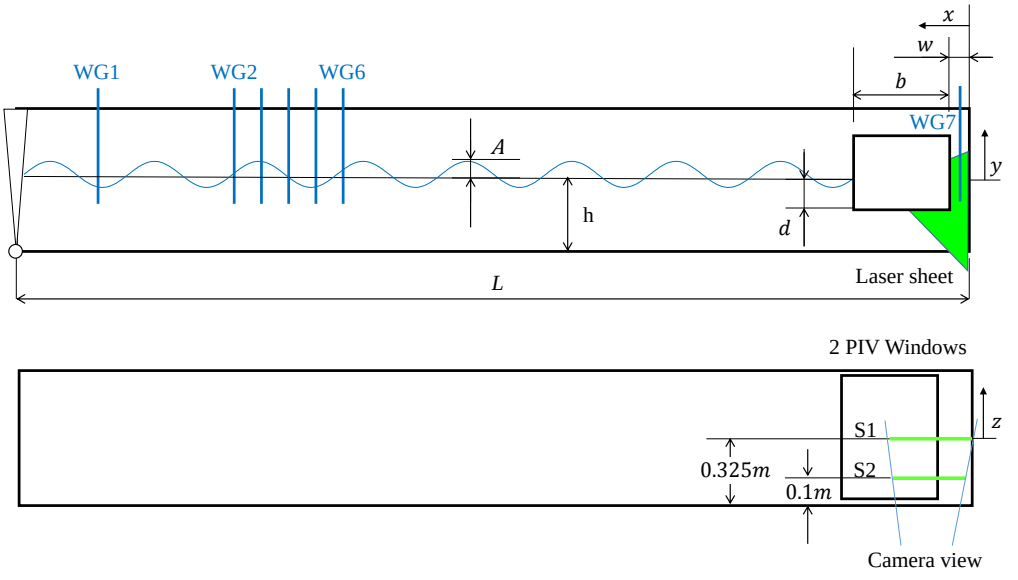

FIGURE 1. Experimental arrangement in the wave tank.

2.2. *Measurement of the flow field*

The flow field around the bilge closest to the wall (i.e. within the gap and below) was observed using a PIV system which comprised two 50 mJ lasers pulsed at 100 Hz. The acquisition frequency was set to 200 Hz by adjusting the interval between the two laser pulses. A Phantom V641 camera with a resolution of 2560 × 1600 pixels was synchronized with the laser pulses. The water was seeded with silver coated hollow glass spheres of around 10 to 14 μm in diameter.

The vorticity ($\omega = \partial v/\partial x - \partial u/\partial y$) was computed using an adaptive PIV algorithm based on that described by Thomas *et al.* (2005). The same algorithm was also applied to compute the vorticity from the CFD velocity data for consistency. The 10-point scheme has the advantage of reducing the effect of fluctuations. A consequence of employing this scheme, however, is that the first two points on the hull wall are subject to a relatively large error. For the smallest discretisation used in the PIV, this affected a region of up to 0.3 mm from the hull wall. The computation of the flow field from the PIV images was also affected by the reflection from the laser sheet onto the hull. As such, it was not possible to reliably compute the flow field in the region of this intense light. This affected a region around 1 mm from the hull, depending on the angle of incidence of the light.

Several fields of view which corresponded to different discretisations (pixel sizes) were tested, as summarised in table 1. For each case, the field was centred on the bilge. Except for the smallest field of view, these images also provided an independent measurement of the free surface in the gap to verify the wave probe measurements. While the majority of the measurements were obtained near the centre of the hull at approximately $z = 0$, where z is in the spanwise direction, data were also obtained at $z = -0.225$ m which allowed for an assessment of spatial variability.

Case	Field of view	Camera pixel size	PIV pixel size
I	494 × 309	0.193	0.772
II	297 × 186	0.116	0.464
III	182 × 114	0.071	0.284
IV	96 × 60	0.037	0.148

TABLE 1. Field and view (width × height) and dimensions of the pixels corresponding to the camera images and PIV measurements. All values are in mm.

3. CFD model

The two-dimensional flow field was predicted using a finite-volume solver for the unsteady Navier-Stokes equations for multi-phase flow (i.e. air-water) using direct numerical simulation (DNS) i.e. with no turbulence model included. Consistent with Lu *et al.* (2020), this was justified based on the flow along the side walls of the gap likely being predominantly in the laminar regime. For a typical case with a wave period $T = 1.1\,\mathrm{s}$, such that $\Omega = 5.71\,\mathrm{rad\,s^{-1}}$ and with the kinematic viscosity $\nu = 1.15 \times 10^{-6}\,\mathrm{m^2\,s^{-1}}$, the thickness of the Stokes oscillatory boundary layer on both the hull and vertical wall would be expected to be $\delta = 2\pi\sqrt{2\nu/\Omega} = 0.6\,\mathrm{mm}$. Taking the gap width as a relevant length-scale, a Stokes parameter may also be formed as $\beta = w^2/\nu T \approx 4200$. The displacement thickness of the Stokes layer/gap is $\delta^*/w = (1-i)\,e^{i\Omega t}/\left(2\pi\sqrt{\beta}\right)$ which has a maximum value of about 0.0025, i.e a very small portion of the gap. The skin friction is similarly proportional to $1/\sqrt{\beta}$ and is very small compared with the pressure drag force from the vortex shedding. Thus this informs the design of the computational mesh, which should be sufficiently fine to capture the vortex shedding while the resolution of the Stokes layers is likely of secondary importance.

The dimensions of the computational domain were equivalent to the experiment in the x, y-plane. The walls of the hull and exterior domain were set as no-slip boundaries with the upper surface of the domain defined as a pressure-outlet. Regular waves were generated at the inlet with a linear ramp function applied to the wave amplitude for the initial three wave periods, as in the experiment. The computations were performed using a fully structured mesh which was refined in the regions of the hull walls, bilges, the vertical end wall and the free surface, as depicted in figure 2. Solutions were attained for three different meshes. These differed between the sizes of the (square) mesh elements which were uniformly distributed within a region of 100 mm × 100 mm centered on the bilge in the gap, as summarised in table 2.

The equations were solved with the widely utilised semi-implicit SIMPLE algorithm (Patankar & Spalding 1972). The second-order upwind scheme was used for spatial discretisation of momentum and the free surface was tracked using the Volume of Fluid (VoF) technique. The computations used a constant time step not exceeding $T/1000$, where T is the wave period. With this, the Courant number was sufficiently low (generally < 1) to ensure simulation accuracy. The free surface time history was extracted at the positions corresponding to the wave gauges in the experiment for comparison with the measurements. The velocity field around the bilge near the wall was sampled at a rate of $T/200$ for comparison with the PIV results.

4. Free surface response

The hydrodynamic response of the free surface in the gap between the hull and wall is first demonstrated, given its central role in driving the vortex shedding around the bilge.

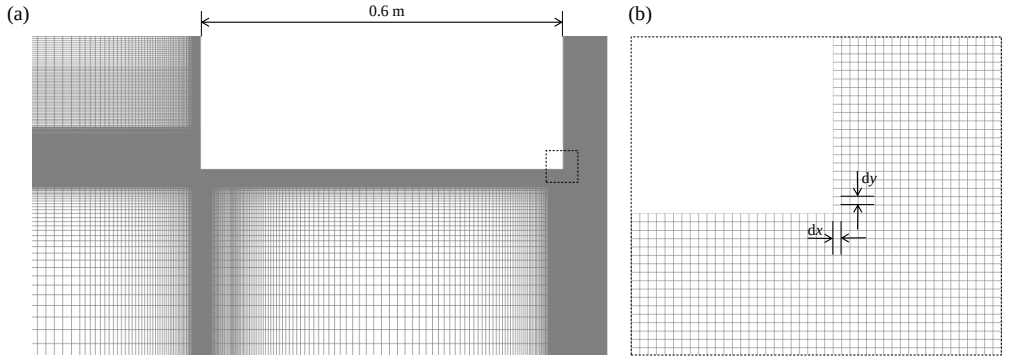

FIGURE 2. CFD mesh; (a) in the region of the hull and wall and (b) in the region of the bilge edge in the gap (bounded by dashed-lines in (a)).

Case	Total elements	Mesh size
A	218475	1.00
B	261100	0.50
C	357600	0.25

TABLE 2. Total mesh elements in the domain and dimensions of the mesh ($dx = dy$, mm) within a 100 mm × 100 mm region centered on the bilge in the gap for the CFD model.

Figure 3(a) shows the gap response amplitude operator (RAO) measured by the wave gauge located at the centre of the gap, as a function of the incident wave period. Here, the $RAO = A_{gap}/A_i$, where A_{gap} is the wave amplitude in the gap and A_i is the incident wave amplitude. The results are for constant wave steepness values of $H/\lambda \simeq 2A_i/\lambda = 1.3\,\%$ and $2.6\,\%$, where λ is the wave length. The resonant peak of the piston mode at a wave period of around $T = 1.15$ s is clearly distinguishable, varying weakly with wave steepness. Figure 3(b) plots the RAOs as function of the wave steepness for a wave period $T = 1.1$ s, thus coinciding close to resonant conditions. The RAO exhibits a decrease with wave steepness at a rate close to $(H/\lambda)^{-1/2}$, consistent with a purely quadratically damped response.

The measurements have initially been compared with predictions from a potential flow model with a damping lid in the gap, based on Molin *et al.* (2009) and applied previously by Kimmoun *et al.* (2011) and Milne *et al.* (2020). In the model the inviscid solution is obtained using a matched eigenfunction expansion method and the force applied to the massless lid located at the surface is of the form $F = -\frac{1}{2}\rho C_{D_L} w|\dot{\eta}|\dot{\eta}$, where η is the free surface elevation in the gap and ρ is the fluid density. Favourable agreement is demonstrated when employing a quadratic damping coefficient of $C_{D_L} = 1.4$ and neglecting the Stokes attached flow contribution. This coefficient was determined through iterative tuning to achieve a best fit to the RAO versus H/λ curve and it is emphasised that its value was the same for all wave periods and steepness. The results suggest that the viscous damping coefficient is independent of the oscillatory amplitude in the gap, thus consistent with the K_C^0 proportionality expected for an infinite isolated right-angled edge (Graham 1980). This is discussed further in Section 6.

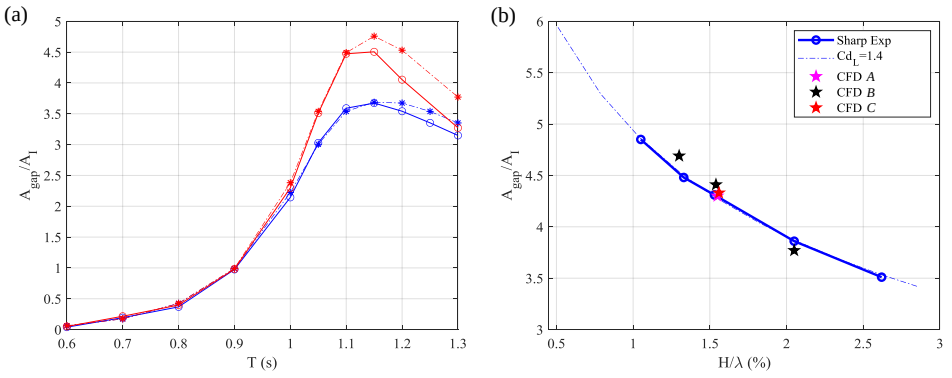

FIGURE 3. Free surface RAOs; (a) as function of wave period for constant wave steepness of H/λ = 1.3 % (blue) and 2.6 % (red), with the dashed-line corresponding to the damping-lid model prediction; (b) as a function of wave steepness for T = 1.1 s with results for both the lid damping model and CFD shown.

Consideration is now given to the comparisons with the CFD results which have been obtained for T = 1.1 s and varying values of steepness. The predicted RAOs are shown to be consistent with the measurements and those attained using the lid damping model. The results for H/λ = 1.6 % corresponding to the three different CFD mesh sizes also serve to show that the computations were satisfactorily converged. As a means of further demonstrating the efficacy of the CFD model, the predicted time histories of the free surfaces at various positions along the tank and in the gap for H/λ = 1.3 % are plotted in figure 4. The computed traces are shown to be generally in close alignment with the measurements.

The incident and the reflected amplitudes were subsequently evaluated from both the measured and computed upstream surface elevation data. Here, the technique of Mansard & Funke (1980) was applied on moving windows two wave periods ($2T$) in width with a translation of $T/10$. Figure 4 shows the time evolutions of these respective wave amplitudes up to the time in which the wave, having reflected from the hull and then reflected from the wave-maker, re-encountered the first wave gauge. Also plotted are the reflected and dissipation coefficients, which are related through energy considerations by $K_d = \sqrt{1 - K_r^2}$. A significant portion (i.e. > 90 %) of the wave energy was dissipated. The agreement between the measured and computed incident wave amplitudes provides confidence in having replicated the onset flow conditions. However, the reflected wave amplitude is over predicted. It is postulated that turbulence which was not explicitly modelled within the numerical solutions, which most likely affects the flow at scales much smaller than those governed by the oscillatory period, may have been the source of the increased dissipation in the experiment.

5. Vortex shedding dynamics

5.1. *Flow around the bilge and in the gap*

The flow around the bilge next to the wall and in the gap for near resonant conditions is now examined. Figure 6 shows the measured and computed instantaneous vorticity contours and velocity vectors over a single cycle once quasi-steady resonant conditions have been attained (but prior to encountering reflected waves) for H/λ = 1.6 % and

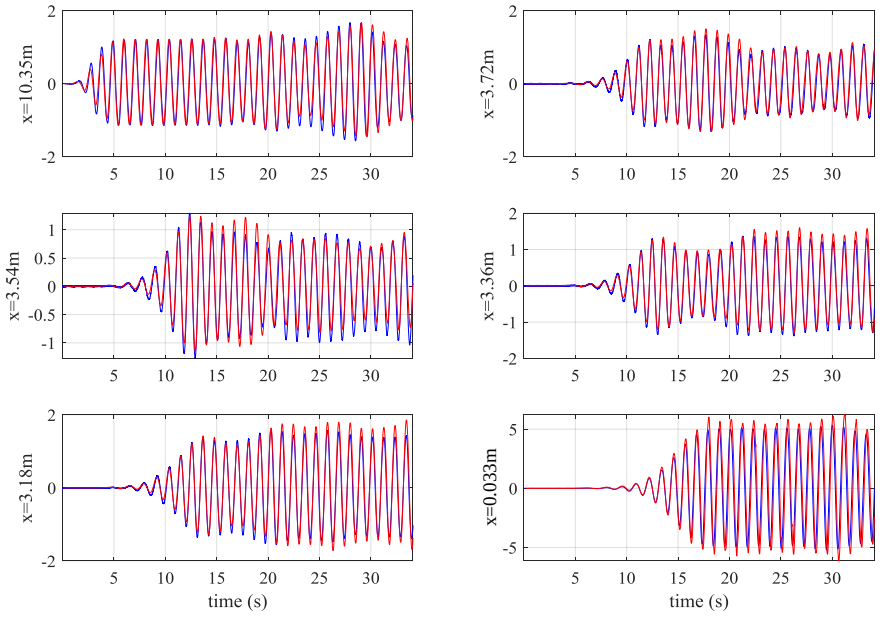

FIGURE 4. Time histories of the measured (blue) and CFD prediction (red) of the free surface elevation (in cm) at various distances upstream from the vertical wall, for T = 1.1 s and H/λ = 1.3 %.

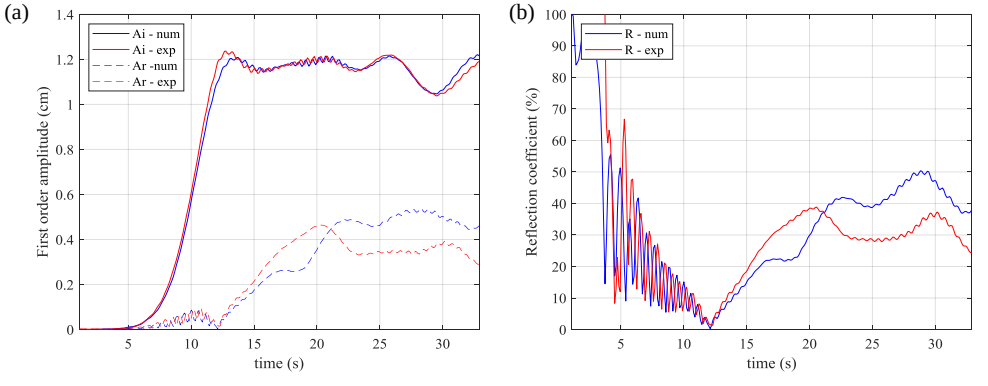

FIGURE 5. (a) Time evolution of the incident and reflected waves amplitudes and (b) reflection coefficients, obtained using the separation method for T = 1.1 s and H/λ = 1.3 %.

T = 1.1 s. The results are at intervals of $T/8$, labelled consecutively, as the flow enters and is then expelled out of the gap. The PIV data are for a pixel size of 0.116 mm (case II), corresponding to 0.462 mm for the PIV algorithm, with the field of view sufficiently large to visualise the flow up to the free surface. The CFD results are for a mesh size of 1.0 mm (case A).

The plots elucidate the inherent complexities in the flow field and the differences compared to shedding around an isolated edge. As the flow enters the gap (occurring between panels 1 and 2) a thin shear layer emanating from the bilge rolls up to form a concentrated counter-clockwise (CCW) vortex core (of negative vorticity and denoted as 'B'). The CCW vortex pairs with a clockwise (CW) vortex ('A', of positive vorticity)

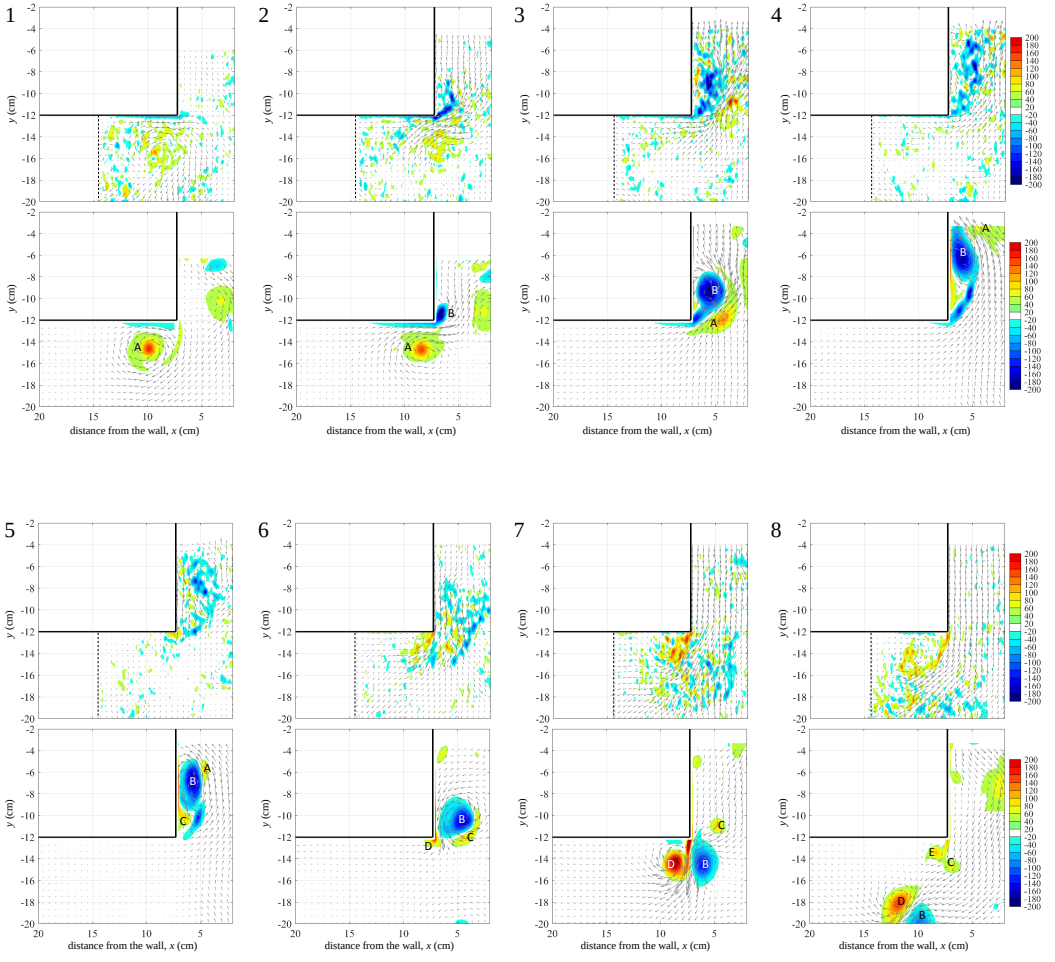

FIGURE 6. Measured (upper panels, for case *II*) and computed (lower panels, case *A*) instantaneous vorticity contours at equivalent intervals of $T/8$ (numbered consecutively) during resonance for H/λ = 1.6 %, T = 1.1 s. The vortex cores are labelled A to E. The extent of the PIV field of view is shown by the dashed lines.

which was shed in the previous half cycle that has entered the gap with the bulk flow. Owing to the restriction imposed by the narrow gap and the presence of the CW vortex, as the CCW vortex expands it remains near the vertical hull wall (panels 3 to 4). This results in an attached flow away from the edge being induced beneath the primary CCW vortex which is now within a system comprising multiple (negative) vortical regions. The attached flow subsequently separates, generating a secondary CW vortex (denoted as '*C*' within panel 5) which initially pairs with core '*B*' and convects upward. Without the secondary separation off the surface new positive vorticity would be shed later from the edge when the flow at the edge reverses. As such, here, there is an additional vortex pair ('*B* – *C*') generated within the system.

The residual positive vorticity which remains attached to the vertical wall is subsequently swept to the edge, forming the next CW vortex ('*D*', in panel 7) below the hull

as the flow reverses. The proximity of this CW vortex to the hull also induces a local attached flow beneath the hull with relatively weak secondary separation. The primary CCW vortex ('B') is ejected from the gap as the free surface is displaced downward. This vortex now pairs with the CW vortex 'D'. The interaction of the vortices, which are of similar but opposite strength, results in a strong local downward velocity below the hull. As the flow reverses again and the free surface moves upward, the CW vortex is reinjected into the gap and the shedding process then repeats. Regions of intense vorticity are present near the hull walls, the thin shear layers and the vortex cores, which are all associated with large flow gradients. Residual vorticity associated with previous shedding cycles is also evident in the flow field, which contributes to the mixing and the decay of the primary vortices.

To demonstrate the consistency of the flow dynamics, figure 7 plots the time histories of the vorticity maxima (both positive and negative) within the field of view and its position relative to the bilge. The corresponding free surface elevation in the gap is also shown for reference. The instances of the most intense positive vorticity are associated with the formation of the concentrated CW vortex core which initially remains just below the bilge. The positive vorticity decreases in strength as the CW core is displaced downward, pairs with the CCW vortex and then moves back upward into the gap. The instances of positive vorticity close to the hull and above the bilge correspond to the local attached flow and the formation of the secondary CW vortex. The secondary separation is also identifiable by the smaller secondary spikes in vorticity maxima time history. Further complexities are exhibited in the negative vorticity. In particular, as the flow enters the gap the maxima alternates between the CCW cores within the multiple vorticial region. Similarly, this gives rise to multiple spikes in the vorticity traces.

5.2. *Sensitivity to discretisation*

The ability to detect flow features such as shear layers, concentrated vortex cores and secondary separation is inherently dependent on the respective CFD and PIV discretisations. This is of particular concern when assessing convergence and, moreover, comparing numerical and measured results. The effect of discretisation on the CFD results is demonstrated first, using the $H/\lambda = 1.6\,\%$, $T = 1.1\,\mathrm{s}$ case again. In the computational results, the discretisation changes the capability of the model to describe the physics. Figure 8 shows the traces of the vorticity maxima, together with the surface elevation in the gap, computed using smaller CFD mesh sizes around the bilge of $dx = 0.50\,\mathrm{mm}$ and $0.25\,\mathrm{mm}$ (i.e. cases B and C). The results are generally consistent with those for the coarser mesh in figure 6. However, the use of a smaller mesh size further elucidates the regions of highly concentrated vorticity close to the hull walls, including those associated with the generation of the secondary vortices.

Figure 9 compares the instantaneous vertical and horizontal velocity maxima computed using the three different mesh discretisations. Importantly, as for the free surface responses in the gap, the computed velocities are shown to be in close alignment. The results therefore indicate that the underlying vortex dynamics within the gap associated with the damping have been resolved and reinforces the particular challenge of demonstrating convergence for a gradient quantity such as the vorticity.

In contrast to the numerical computations, changing the PIV resolution and the field of view modifies the ability to capture the structures while the background physics should be equivalent. The effect of the discretisation on the measured vorticity is demonstrated in figure 10. The larger peaks in the positive vorticity for enhanced PIV resolutions imply greater refinement of the gradients associated with the CW vortex cores below the bilge. The negative vorticity is comparatively less sensitive to the resolution but

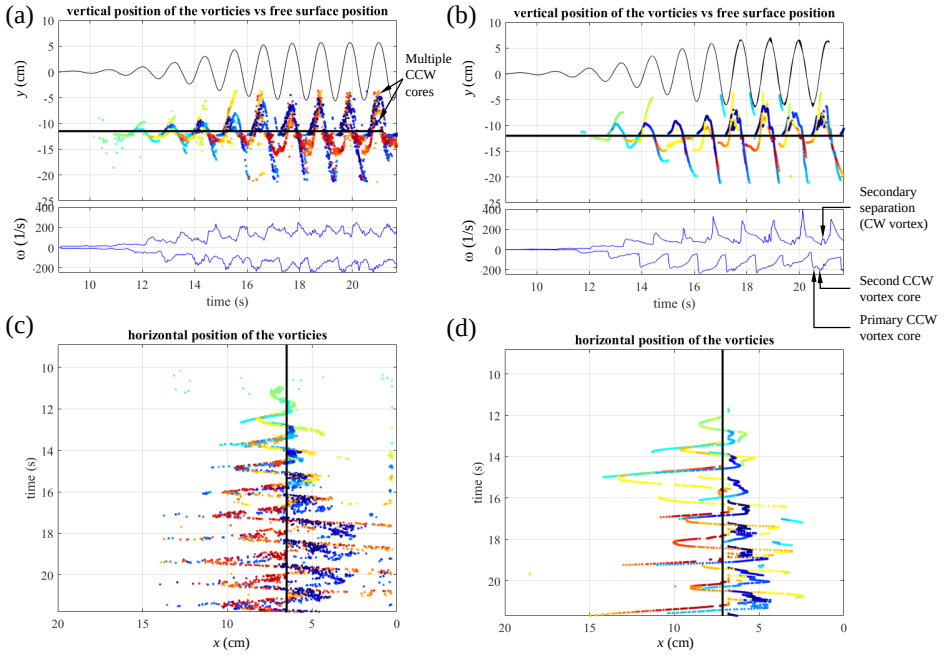

FIGURE 7. Vertical and horizontal positions of the vorticity maxima in the gap measured for case *II* (panels (a) and (c)) and computed using mesh case *A* (panels (b) and (d)) for $T = 1.1\,\mathrm{s}$ and $H/\lambda = 1.6\,\%$. The colour range corresponding to the intensity of the vorticity is consistent with figure 6. The free surface elevation in the gap and the edges of the hull are shown by the respective thin and thick solid lines. The vorticity intensity is also shown in panels (a) and (c) for reference.

which is attributed to the thin shear layers and highly concentrated CCW cores within the multiple vortical region which are beyond the limits of the PIV system to resolve. Figure 11 shows that similar to the numerical computations the velocities measured using the different PIV resolutions agree well. However, since the horizontal velocity maxima can occur further away from the bilge compared to the vorticity maxima there are instances (most evident around the secondary peaks) where those results are affected by the differing fields of view.

Collectively, these insights are particularly valuable when validating numerical computations using measured data. Direct comparisons of the vorticity and vertical velocity maxima between mesh *B* and PIV case *III* and between mesh *C* and PIV case *IV*, respectively, are made in figure 12. To facilitate the evaluations, here the CFD results are for a field of view equivalent to the PIV. For these cases, the respective discretisations are shown to have enabled near equivalent resolution of the shedding dynamics associated with the positive vorticity. The limitations of the PIV to fully resolve the features associated with the negative vorticity maxima is again highlighted in the comparisons with the finest CFD mesh. As the negative vorticity in the vortex system is particularly sensitive to the secondary separation, it could however be expected that obtaining agreement between the measurements and computations is inherently challenging. The computed and measured velocities, which are less sensitive to both mesh and PIV discretisation, are shown to align closely and provide additional support for having replicated the experiment numerically.

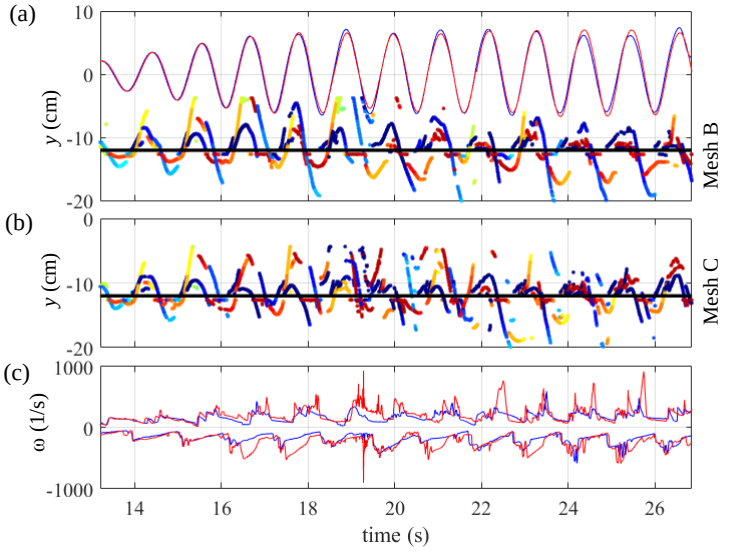

FIGURE 8. Vorticity maxima computed in CFD using mesh sizes of 0.50 mm (case B) and 0.25 mm (case C), for T = 1.1 s and H/λ = 1.6 %. The vertical positions of the vorticity maxima for the respective cases are shown in panels (a) and (b) for clarity, with the colour ranges consistent with figure 6. The traces of the free surface elevation in the gap and vorticity intensity are shown in (a) and (c), for reference, where case B is plotted in blue and case C in red.

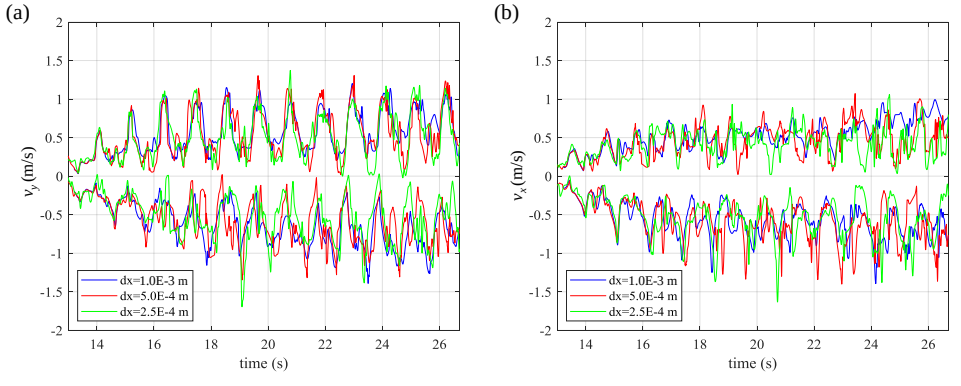

FIGURE 9. Comparison of the computed (a) vertical and (b) horizontal velocity maxima using different CFD mesh resolutions for T = 1.1 s and H/λ = 1.6 %.

5.3. *Secondary separation mechanisms*

Secondary separation which leads to the generation of multiple vortex systems appears to be an attribute of resonant gap flows. It is similar to the secondary separation which is observed under the primary vortices which form above sharp leading edges of delta wing aircraft at high angles of attack (see, e.g. Luckring (2019)). As the phenomena have not been reported in oscillatory flows around bilges and other edges, the mechanisms of the secondary vortex separation adjacent to the vertical hull wall are further examined here.

Figure 13 shows the instantaneous vorticity contours and velocity vectors computed in CFD using a mesh sizing of dx = 0.50 mm (case B) as the flow enters the gap. The plots

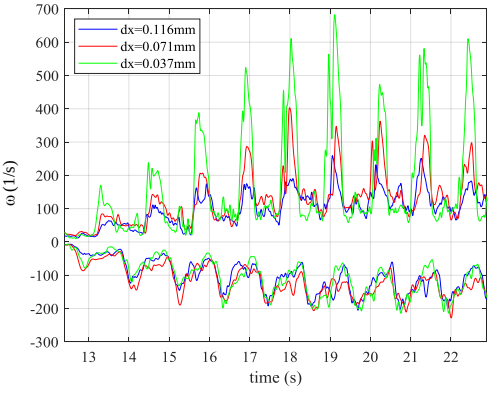

FIGURE 10. Comparison of the measured vorticity maxima using different field of views and pixel sizes for $T = 1.1\,\mathrm{s}$ and $H/\lambda = 1.6\,\%$.

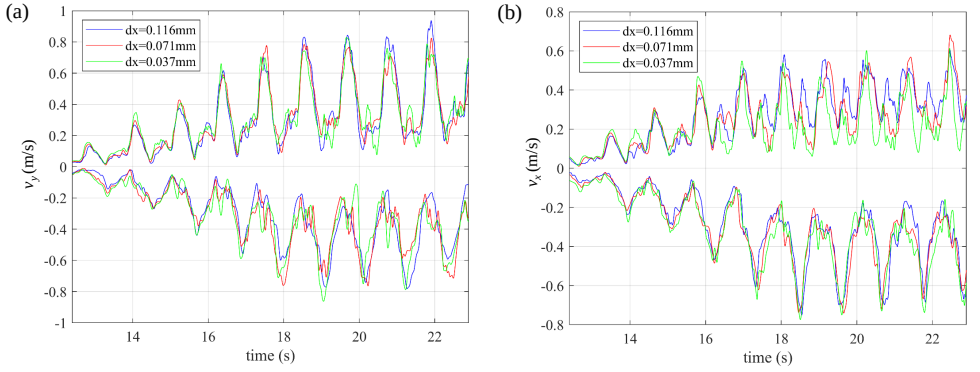

FIGURE 11. Comparison of the measured (a) vertical (b) horizontal velocity maxima using different field of views and pixel sizes for $T = 1.1\,\mathrm{s}$ and $H/\lambda = 1.6\,\%$.

thus provide enhanced resolution of the inherent complexities in the vortex shedding compared to figure 6. Specifically, the CW vortex ('C') which is formed following the separation of the attached flow away from the edge is shown to pair with the primary CCW vortex ('B') with residual vorticity remaining on the hull wall. The pair ('$B-C'$') initially convect away from the hull and towards the vertical wall and then upwards within the gap, with the CW vortex rotating above the CCW core. The smaller CCW vortex ('b') is instead displaced around the bilge, pairing with the CW vortex 'D' during its formation, before the primary CCW vortex is ejected from the gap. Evidence of the secondary separation and formation of multiple cores is also present in the PIV measurements obtained using 0.071 mm pixels (case III), though notably only part of the primary vortex is able to be visualized within the field of view.

As demonstrated by Hummel (1979) for a delta wing, the surface pressure distributions also serve to help inform the separation dynamics. The corresponding instantaneous static pressure distributions along the vertical hull wall computed using CFD are also shown in figure 13. The peaks in the suction associated with the primary and secondary vortices are identifiable. Also evident is the region of the adverse pressure gradient which results in the separation of the attached local flow (induced by the primary vortex and directed

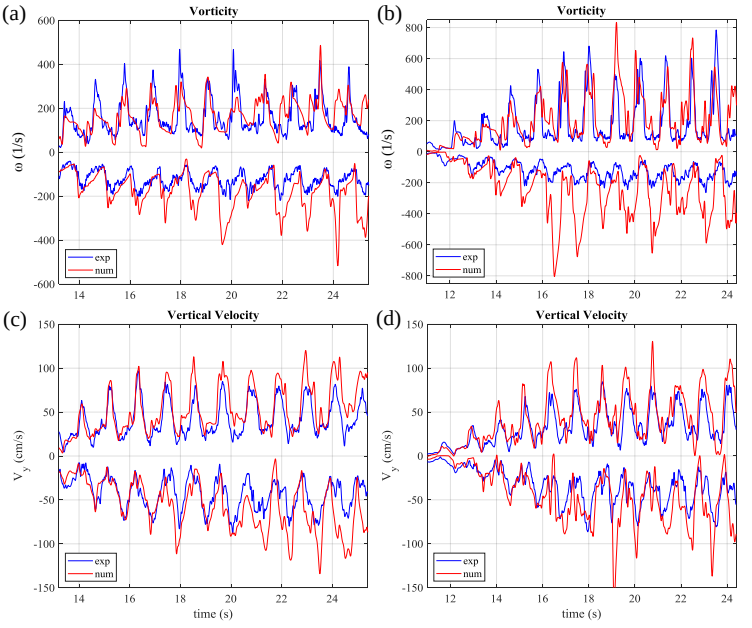

FIGURE 12. Comparison of the computed and measured vorticity and vertical velocity maxima for T = 1.1 s and H/λ = 1.6 %. (a,c) PIV with pixels of 0.071 mm (case III) and CFD with a mesh size of dx = 0.50 mm (case B); (b,d) PIV with pixels of 0.037 mm (case IV) and CFD with a mesh size of dx = 0.25 mm (case C).

towards the edge), forming the secondary CW vortex. The displacement of the primary core initially shifts the location of this adverse pressure gradient upward towards the free surface.

Figure 14 plots the trajectories of the largest vortex structures computed in CFD using dx = 0.50 mm (case B) to further illustrate the interactions. Specifically, the primary CCW and CW vortices and the secondary CW vortex have been tracked from their initial formation until they diffuse or are longer visible within the field of view. Their locations at time $t = 20T$ and $21T$, with respect to the start of the simulation, are also indicated for reference. The interaction between the primary CCW vortex and secondary CW vortices, once the latter has formed, is particularly evident. While the primary CCW vortex is ultimately ejected from the gap, the secondary CW vortex reenters the gap and decays within it.

5.4. *Self-similarity and spatial invariance*

Finally, consideration is given to the variability in the shedding dynamics with the forcing amplitude and along the span of the barge. The spanwise variability, in particular, has seldom been previously reported for gap resonance studies. The measured vorticity maxima for varying wave steepness, based on a pixel size of 0.071 mm (case III) are compared in figure 15(a). The results demonstrate that the underlying vortex dynamics were generally consistent in the range $1.06 < H/\lambda \leq 1.62$ %, including exhibiting secondary separation. Figure 12(b) plots the vorticity maxima for a relatively large steepness of H/λ = 2.6 %. The significant surface amplitudes in the gap necessitate the use of a larger field of view in the PIV (case I), at the expense of a reduction in the resolution. However, the spatial homogeneity is evident in the comparisons of the measurements which were repeated at the two different spanwise locations. This spanwise spatial invariance also

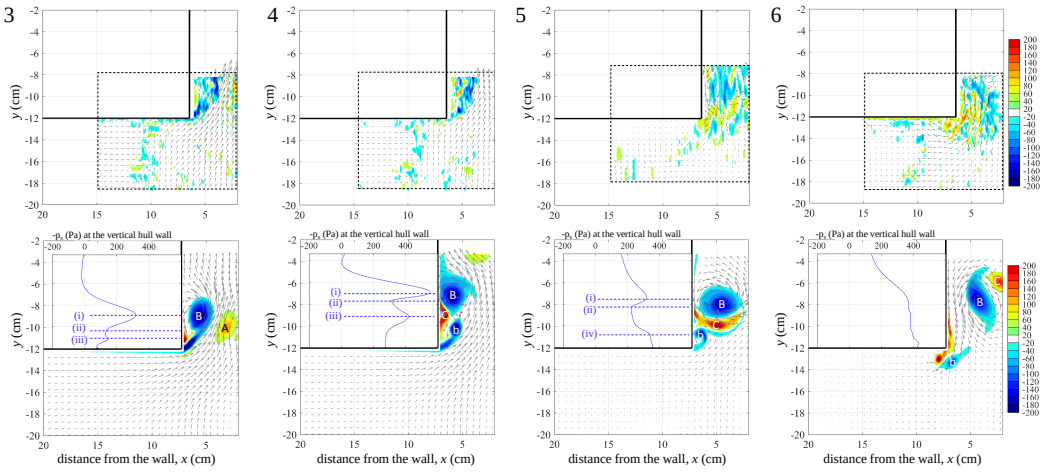

FIGURE 13. Measured (upper panels, for case *III*) and computed (lower panels, case *B*) instantaneous vorticity contours at equivalent intervals of $T/8$ (numbered consecutively) during resonance for $H/\lambda = 1.6\,\%$, $T = 1.1\,\mathrm{s}$. The vortex cores are labelled to be consistent with figure 6, with the smaller cores also identified in lowercase. The extent of the PIV field of view is shown by the dashed lines. The surfaces pressures ($-p_s$ (Pa)) along the vertical hull wall computed in CFD are shown in the insets with key features labelled. The peaks at (i) correspond approximately to the primary CCW core. An adverse pressure gradient exists between (i) and the location of the secondary separation (ii). The CW vortex core associated with the secondary separation is at (iii) and the secondary CCW vortex core corresponds to (iv).

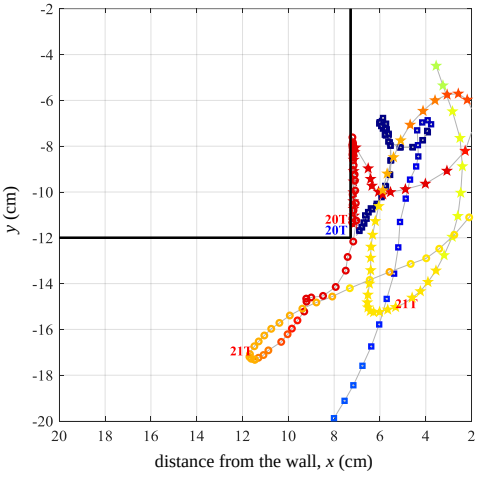

FIGURE 14. Trajectories from formation of the vortices '*A*' (∘), '*B*' (□), '*C*' (⋆), as identified in figure 13. The vorticity colour range is consistent with figure 6 and the positions of the vortices at time $t = 20T$ and $21T$ are labelled for reference.

suggests that the process by which the vortex is shed from the bilge is approximately two-dimensional. On this basis, it is postulated that three-dimensionality only becomes significant once the vortices are relatively small in size and are in the process of decaying.

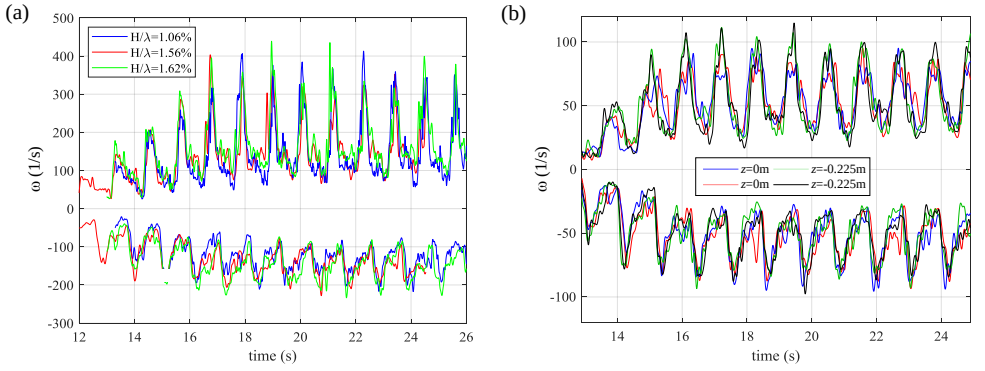

FIGURE 15. Measured vorticity maxima for $T = 1.1\,\mathrm{s}$, (a) as a function of wave steepness and (b) as repeated at two different sections of the barge for $H/\lambda = 2.6\,\%$.

Moreover, this provides justification for the application of two-dimensional numerical models when predicting the response.

6. Insights from an inviscid discrete vortex model

The vortex contribution to the effective damping of the gap response may also be assessed using an inviscid discrete vortex model (DVM). It is applied for the present analysis to an idealised two-dimensional geometry of one end of a semi-infinite rectangular hull separated from an infinite vertical wall by a small gap. Since the flow field is assumed inviscid it may be represented by a velocity potential which satisfies Laplace's equation and is invariant under conformal transformation. Transforming the geometry to a half-plane bounded by a wall on one side allows a simple representation of the vortex shedding by a sequence of discrete vortices and their images in the plane boundary. This method follows the procedure of many discrete vortex methods including that for an isolated sharp edge in oscillatory flow (Graham 1980).

The flow field in the physical $z\,(= x + iy)$ plane surrounding the rectangular hull section and vertical wall is transformed into the lower half $\zeta\,(= \xi + i\eta)$ plane by the Schwartz-Christoffel transformation:

$$\frac{\partial z}{\partial \zeta} = \frac{\sqrt{\zeta^2 - \xi_e^2}}{\zeta} \tag{6.1}$$

which can be integrated to give

$$z = \sqrt{\zeta^2 - \xi_e^2} - \xi_e \tan^{-1}\left(\frac{\sqrt{\zeta^2 - \xi_e^2}}{\xi_e}\right) + z_e \tag{6.2}$$

Here z_e is the location in the z-plane and ξ_e the corresponding point on the real axis in the ζ-plane, of the sharp right-angle edge of the hull, with the wall located on the line $\xi = 0$. The bottom of the hull lies along the real z axis and the far edge is at $x = \infty$.

Equation 6.1 has been derived requiring that $\frac{\partial z}{\partial \zeta} \to 1.0$ as $\zeta \to \infty$ so that conditions far from the edge region are preserved. The free surface region as $y \to \infty$ with $x \sim 0$ in the z-plane corresponds to the origin in the ζ-plane. It is convenient to set the gap width w to be unity so that all lengths are non-dimensionalised by the gap width and to also set the vertical velocity amplitude V_{mfs} of the free surface (at $y \to \infty$ in the

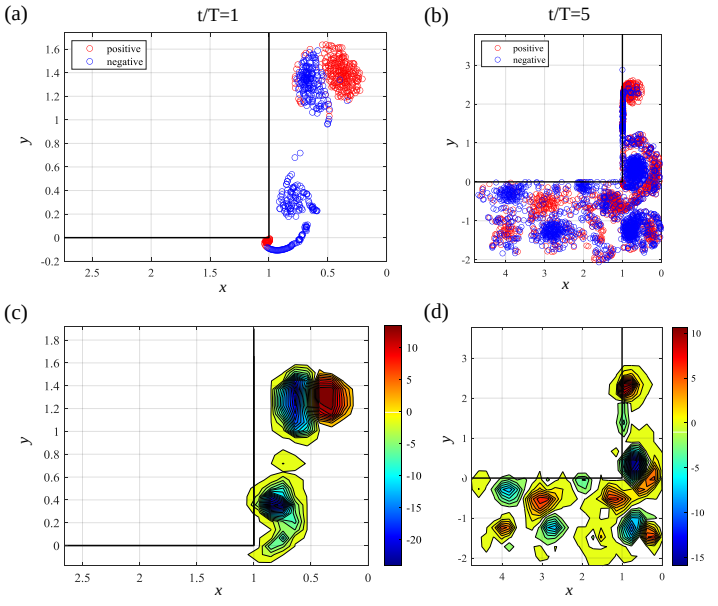

FIGURE 16. Discrete vortex distributions (a, b) and corresponding vorticity contours (c, d) for $t/T = 1$ and $t/T = 5$.

gap) to unity so that all velocities are non-dimensionalised by this velocity. Therefore, in the ζ-plane the free surface flow must be represented by a source m at $\zeta = 0$ which, in order to provide the correct instantaneous volume flow rate in the gap, together with image considerations, requires $m(t) = 4wV_{mfs}e^{i\Omega t} = 4e^{i\Omega t}$, since only one quadrant of the actual source flows into the physical gap. To be consistent with these values $\xi_e = 2/\pi$. The wave height (or double amplitude) H in the gap and the gap width w are the only length-scales in this simplified problem. The flow field evolving in non-dimensional time, t/T, is therefore specified by a single parameter, H/w the length-scale ratio. The solution proceeds by discrete time-steps (=0.01 in non-dimensional units) with a new vortex shed at each time-step so that the Kutta-Joukowski condition is satisfied at the sharp edge which is the shedding point. Shed vortices are then convected according to the local velocity at their locations in the physical plane.

A parametric study was carried out for a range of values of H/w. Examples of the vortex shedding are shown in figure 16 in the form of plots of the discrete vortex distributions and corresponding vorticity contours. The effective force acting on the flow due to the shedding of vortices from the edge is evaluated by computing the additional pressure acting at the free surface caused by the vortex shedding. The additional pressure at the mean free surface due to vortex shedding is given by $\Delta p = -\rho d\phi/dt$ where ϕ being invariant under the transformation is the value of the real part of the complex potential W(due to the vortices) in the ζ-plane as $\zeta \to 0$ (the additional contribution from the vortices to the velocity squared term being negligible at the free surface). Integrating this additional pressure over the free surface in the gap gives the additional force coefficient $C_F = \Delta p/\frac{1}{2}\rho V_{mfs}^2$ acting at the free surface due to the vortex shedding. A constant coefficient with this Morison definition implies quadratic damping which is equivalent to a conventional (linearly non-dimensionalised) wave-diffraction theory damping coefficient which increases linearly with wave amplitude. Figure 17 plots C_F as a time sequence over

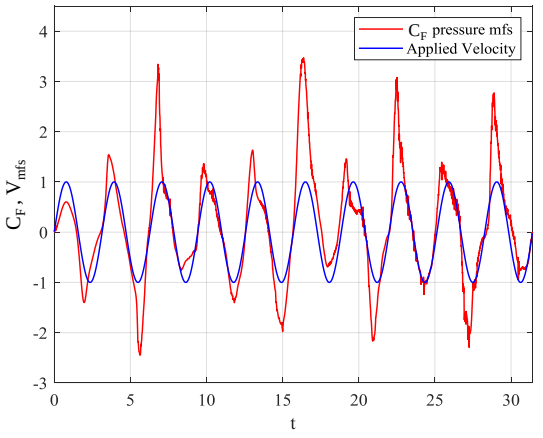

FIGURE 17. Force coefficient time history computed using DVM.

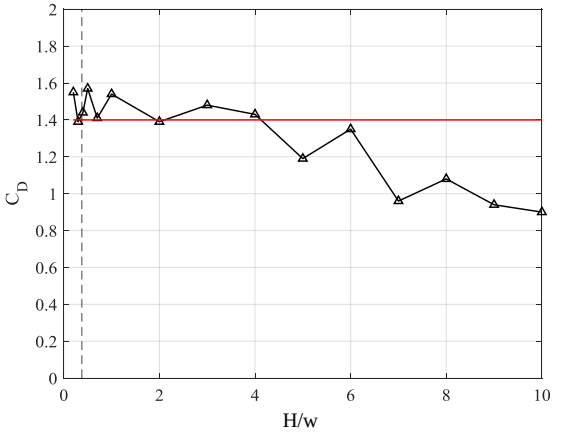

FIGURE 18. Vortex drag coefficient dependency computed using DVM. The continuous red line indicates the empirical value of C_D used for the damping lid model computations. The dashed line corresponds to the value of H/w for the experiment, damping lid model and CFD results.

10 cycles of flow. This shows that the vortex force is strongly in phase with the velocity which is as predicted for an isolated right-angle edge, the contribution from the inertia force (that part of the force in phase with the free-surface acceleration) being extremely small (Graham 1980). Obtaining the component acting in phase with the free surface velocity gives the effective damping coefficient C_D acting on the free surface in the gap. In all other far field directions the pressure field due to the vortex shedding decays to zero with distance fast enough to give no contribution.

Results for C_D calculated in this way are shown for a range of H/w from 0.2 to 10.0 in figure 17. Also marked in this figure is the empirical value C_D = 1.4 which was applied to the inviscid diffraction computation to give close agreement with the peak value of the resonant RAO in the gap. C_D for the isolated edge as predicted by theory (Graham 1980) shows that the dependency on Keulegan-Carpenter number should be $K_C^{2/(3-2\delta/\pi)-1}$ which implies independence of K_C and hence flow amplitude when, as here, the internal edge angle $\delta = \pi/2$. In the present case of an edge close to a vertical

wall for small amplitudes of water vertical displacement in the gap C_D is approximately independent of changes in H/w. For $H/w > 3.0$ the effect of the vortex confinement in the gap as H/w increases gradually depresses the values of the drag coefficient below the small amplitude value. The value of the empirical damping coefficient $C_D = 1.4$ used in the diffraction computations compares well with the average value of the damping coefficient shown in figure 18. While this inviscid computation can therefore generate useful estimates of vortex effect for separation from a sharp edge it cannot of course predict secondary separation nor the effects of rounding of a bilge in leading to complete or partial suppression of separation.

7. Conclusion

A new series of wave tank experiments and the application of computational models of varying fidelity have provided new insights into the resonant flow in a narrow gap between a stationary hull and a vertical wall. Vortex shedding from the sharp bilge edge of the hull has been demonstrated to give rise to a quadratically-damped free surface response in the gap at resonance. The shedding dynamics were found to exhibit a high degree of invariance to the amplitude in the gap and spatial uniformity along the span of the barge. Secondary separation was also identified as a particular feature of the separated flow at the hull bilge which led to the generation of a system with multiple vortical regions and asymmetries between the inflow and outflow.

The findings can assist in improving or accelerating the computational methods used to predict resonant gap flows and inform offshore operations such as the side by side offloading from FLNG. The influence of discretisation has been demonstrated to be a particularly important consideration when studying the flow dynamics within the gap and comparing flow quantities between PIV and CFD. While it was shown that the instantaneous velocity maxima were well converged both experimentally and numerically, demonstrating convergence and agreement in the gradient quantities such as vorticity is likely to be more challenging. This is attributed to the concentrated vortex cores, thin shear layers and the complexities associated with the secondary separation. The study has also reinforced the value of more computationally efficient semi-empirical models for accounting for the vortex-induced damping in gap flows, provided their limitations are acknowledged. Using both a damping-lid model and a novel application of a discrete vortex model it has been demonstrated that universal quadratic-damping coefficients, independent of wave steepness and frequency, may be able to be determined. Such computations are well suited to parametric studies and therefore can be useful for facilitating initial operability assessments, though obviously do not directly model secondary separation.

Acknowledgment

This research was supported by the ARC Industrial Transformation Research Hub for Offshore Floating Facilities which is funded by the Australian Research Council, Woodside Energy, Shell, Bureau Veritas and Lloyds Register (Grant No. IH140100012).

The authors report no conflict of interest.

REFERENCES

Faltinsen, O.M. & Timokha, A.N. 2015 On damping of two-dimensional piston-mode sloshing in a rectangular moonpool under forced heave motions. *J. Fluid Mech.* **772**, R1.

Feng, X., Bai, W., Chen, X.B., Qian, L. & Ma, Z.H. 2017 Numerical investigation of viscous effects on the gap resonance between side-by-side barges. *Ocean Eng.* **145**, 44–58.

Graham, J. M. R. 1980 The forces on sharp-edged cylinders in oscillatory flow at low Keulegan-Carpenter numbers. *J. Fluid Mech.* **97** (2), 331346.

Hummel, D. 1979 On the vortex formation over a slender wing at large incidence. In *AGARD-CP-247 Paper 15*.

Kimmoun, O., Molin, B. & Oikonomidou, H. 2011 Wave drift force on a rectangular barge by a vertical wall. In *Proc. 26th IWWWFB, Athens*.

Kristiansen, T. & Faltinsen, O.M. 2008 Application of a vortex tracking method to the piston-like behaviour in a semi-entrained vertical gap. *Appl. Ocean Res.* **30** (1), 1–16.

Kristiansen, T. & Faltinsen, O. M. 2009 Studies on resonant water motion between a ship and a fixed terminal in shallow water. *ASME. J. Offshore Mech. Arct. Eng.* **131** (2), 021102.

Kristiansen, T. & Faltinsen, O. M. 2012 Gap resonance analyzed by a new domain-decomposition method combining potential and viscous flow DRAFT. *Appl. Ocean Res.* **34**, 198–208.

Lu, L., Tan, L., Zhou, Z., Zhao, M. & Ikoma, T. 2020 Two-dimensional numerical study of gap resonance coupling with motions of floating body moored close to a bottom-mounted wall. *Phys. Fluids* **32** (9), 092101.

Luckring, J. M. 2019 The discovery and prediction of vortex flow aerodynamics. *Aeronaut. J.* **123** (1264), 729–804.

Mansard, E.P.D. & Funke, E.R. 1980 The measurement of incident and reflected spectra using a least squares method. In *17th International Conference on Coastal Engineering, March 23-28, Sydney, Australia*, pp. 154–172.

Milne, I. A., Kimmoun, O., Molin, B. & Graham, J. M. R. 2020 An experimental and numerical study of the vortex shedding dynamics during gap resonance. In *Proc. 35th IWWWFB, South Korea*.

Molin, B., Remy, F., Camhi, A. & Ledoux, A. 2009 Experimental and numerical study of the gap resonances in-between two rectangular barges. In *Proc. 13th Congress of Intl. Maritime Assoc. of Mediterranean (IMAM), Istanbul*.

Molin, B., Zhang, X., Huang, H. & Remy, F. 2018 On natural modes in moonpools and gaps in finite depth. *J. Fluid Mech.* **840**, 530554.

Moradi, N., Zhou, T. & Cheng, L. 2015 Effect of inlet configuration on wave resonance in the narrow gap of two fixed bodies in close proximity. *Ocean Eng.* **103**, 88–102.

Patankar, S.V & Spalding, D.B 1972 A calculation procedure for heat, mass and momentum transfer in three-dimensional parabolic flows. *Int. J. Heat Mass Transf.* **15** (10), 1787–1806.

Peri, M. & Swan, C. 2015 An experimental study of the wave excitation in the gap between two closely spaced bodies, with implications for LNG offloading. *Appl. Ocean Res.* **51**, 320–330.

Ravinthrakumar, S., Kristiansen, T., Molin, B. & Ommani, B. 2019 A two-dimensional numerical and experimental study of piston and sloshing resonance in moonpools with recess. *J. Fluid Mech.* **877**, 142166.

Tan, L., Lu, L., Tang, G.-Q., Cheng, L. & Chen, X.-B. 2019 A viscous damping model for piston mode resonance. *J. Fluid Mech.* **871**, 510533.

Thomas, M., Misra, S., Kambhamettu, C. & Kirby, J. T. 2005 A robust motion estimation algorithm for PIV. *Meas. Sci. Technol.* **16** (3), 865–877.

Wang, H., Wolgamot, H. A., Draper, S., Zhao, W., Taylor, P. H. & Cheng, L. 2019 Resolving wave and laminar boundary layer scales for gap resonance problems. *J. Fluid Mech.* **866**, 759775.

Zhao, W., Milne, I. A., Efthymiou, M., Wolgamot, H. A., Draper, S., Taylor, P. H. & Eatock Taylor, R. 2018 Current practice and research directions in hydrodynamics for FLNG-side-by-side offloading. *Ocean Eng.* **158**, 99 – 110.

Zhao, W., Wolgamot, H. A., Taylor, P. H. & Eatock Taylor, R. 2017 Gap resonance and higher harmonics driven by focused transient wave groups. *J. Fluid Mech.* **812**, 905939.